DELPHI Collaboration DELPHI 98-147 PHYS 791
3 August 1998

Photon Analysis with STIC

E. Falk, V. Hedberg
Department of Physics, University of Lund, Lund, Sweden
P. Ferrari, C. Matteuzzi
Sezione INFN, Milano, Italy

Abstract

The calorimeter STIC has been used, for the first time, to identify and analyse events with a photon in the very forward region of DELPHI. Samples of single-photon events were analysed for the reaction $e^+e^- \to \gamma +$ invisible at center-of-mass energies of 161, 172 and 183 GeV. The single-photon events were used to explore the possibilites of using STIC to identify photons while maintaining control over difficult background situations, caused by large amounts of misidentified off-energy electrons and of photons from radiative Bhabha scattering and Compton scattering. In particular, two subdetectors of STIC were used for this purpose: the veto counters, which were used to distinguish photons from electrons, and the silicon-strip detectors, which were tested as a means of rejecting off-energy electron background. The measured cross sections were used to count the number of neutrino generations.

1 Introduction

The calorimeter STIC has been used, for the first time, to analyse events with a photon in the very forward region of DELPHI. The aim of the analysis was to explore the possibilities of using STIC to identify photons and to investigate the means to maintain control over difficult background situations. The analysis was carried out on single-photon events, i.e., for the reaction $e^+e^- \to \gamma +$ invisible, where the photon had entered STIC. Data taken at center-of-mass energies of 161, 172 and 183 GeV were used.

Within the Standard Model, the process $e^+e^- \to \gamma +$ invisible receives contributions from radiative production of neutrino-antineutrino pairs through radiative return to the Z^0 and from t-channel W exchange, with the photon radiated from the beam electron or from the exchanged W. Therefore, single-photon events can be used to count the number of light neutrino generations, N_ν. Although the cross section for radiative neutrino production is rather small, it is very sensitive to N_ν, and this method of measuring the number of neutrino families provides a complement to the so-called lineshape method used at LEP1. Possible contributions to the single-photon final state could also come from some other neutral weakly interacting particle or from a new particle decaying into a photon. Hence, the $\gamma +$ invisible final state also provides a tool to explore the possible existence of new particles.

The measured cross sections for the process $e^+e^- \to \gamma +$ invisible in the present analysis were used to count the number of neutrino families, under the assumption that the only contribution to the single-photon final state comes from the reaction $e^+e^- \to \gamma\nu\bar{\nu}$. Searches for new particles are not reported here. Instead, the analysis of the data at $\sqrt{s} = 183$ GeV is part of a larger analysis, which does include searches for new particles, and in which all three DELPHI calorimeters, STIC, FEMC and HPC, were used [1]. Measurements of this type have been made previously with the HPC calorimeter, for center-of-mass energies between the Z^0 peak and 172 GeV [2]. It is, however, the first time that such measurements have been performed with STIC.

The single-photon data recorded at small polar angles contain large amounts of background in the form of misidentified off-energy electrons, produced in interactions between beam particles and residual gas molecules in the beam pipe, and from radiative Bhabha scattering and Compton scattering, where the electrons escape detection. Even after an event selection defining events with the appropriate single-photon configuration had been carried out, the data samples contained several thousand background events for every true single-photon event. The principal challenge of the single-photon analysis with STIC was to reduce the large background to a level where a meaningful identification of single-photon events became possible. Two subdetectors of STIC were specifically used as tools to reject background: the veto counters, a set of scintillator counters, were used to distinguish photons from electrons; and the silicon-strip detectors were tested as a means to reduce off-energy electrons.

2 The STIC Detector

2.1 The Calorimeters

The luminosity monitor STIC in DELPHI consists of two lead-scintillator calorimeters of shashlik type, read out by wavelength-shifting fibers. These are located on either side of the interaction point at a distance of 2.2 m and have a thickness of about 27 radiation lengths (see Figure 1). Each calorimeter is divided into 10 rings and 16 sectors in such a manner that they form 160 towers that point to the interaction region. The calorimeters are usually referred to as arm A and arm C, according to the DELPHI convention of calling the side of incoming electrons side A and that of positrons side C. For a complete description of these detectors, see [3].

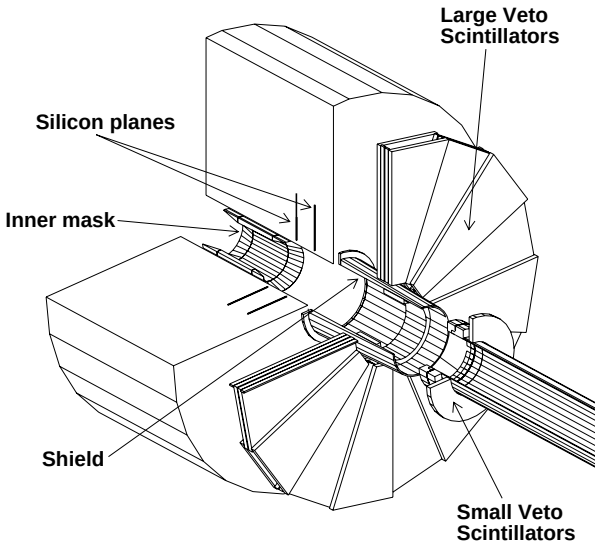

Figure 1: Outline of a STIC calorimeter. The planes of silicon-strip detectors inserted into the calorimeter are shown in the drawing. Placed in front of the calorimeter are the scintillators of the veto-counter system. The inner, or synchrotron, mask, and the shield are tungsten rings that protect the TPC from synchrotron radiation.

The calorimeters extend radially from 65 mm to 417.5 mm, measured from the beam line. This corresponds to a polar-angular acceptance of 29 to 188 mrad (1.7°–10.8°). In reality, however, the inner acceptance is determined by a system of tungsten masks and shields mounted in front of STIC. Some of these were used to define the acceptance in the luminosity measurements at LEP1; others protect the TPC from synchrotron radiation. The configuration of these masks and shields has varied from year to year [4]. For the period covered by this analysis, the inner acceptance was at a radius of 84 mm (2.2°).

2.2 The Veto Counters and the STIC Triggers

A veto system consisting of a set of scintillators is mounted in front of each arm of STIC. This veto system is part of a neutral trigger that provides electron-photon separation. Photons are identified by the absence of signals in the scintillators in front of the point where a showering particle entered STIC.

The scintillator counters are made up of two parts: the main detector, called the large veto counters, and an extension to cover small polar angles, the so-called small veto counters. The large veto counters consist of two layers of scintillator mounted in front of each arm of STIC and covering radii from 96 to 412 mm. The scintillator planes are divided into 16 sectors that match the segmentation of the calorimeters. The small veto counters consist of one layer of scintillator divided into two half-rings that are mounted directly on the beam pipe on either side of the interaction point, in front of the large veto counters. The small veto counters extend radially from 56.5 mm to 130 mm.

STIC provides a so-called single-arm trigger, which requires an electromagnetic shower in one of the arms of STIC, with an energy deposit $E \geq 0.16 E_{\mathrm{beam}}$, where E_{beam} is the beam energy, and with the showering particle entering at a radius $r > 10$ cm. This trigger is used to select and monitor off-energy electron background. The neutral trigger requires the same conditions to be fulfilled as in the case of the single-arm trigger. In addition to this, there is a requirement for the absence of any signal in at least one of the scintillator planes in the region in front of the point where the showering particle entered the calorimeter. In the large veto counters, this region is confined to the sector in which the particle entered STIC, and the two adjacent sectors. In the region of the small veto counters, there is no matching between the scintillator half-rings and the calorimeter sectors, and in order to fulfill the requirements for the neutral trigger, neither half may register a signal. The neutral trigger is fully efficient for energies above 35 GeV [4].

2.3 The Silicon-Strip Detectors

Each calorimeter has been equipped with two planes of silicon-strip detectors with which the direction of a shower can be measured. The purpose of this tracking device is to improve rejection of off-energy electron background. The silicon detectors consist of planes of circular strips replacing one lead-scintillator layer at a depth of 4.0 radiation lengths and another at 7.4 radiation lengths in each of the two arms of STIC, thus giving a total of four silicon planes (see Figure 1). The silicon planes cover 32–77 mrad in polar angle (71.5–174.2 mm and 73.2–178.4 mm in radius respectively). Each silicon plane is divided into 16 sectors that follow the sector geometry of the calorimeter. For a more detailed description of these detectors, see [5].

3 Event Selection

The analysis of single-photon events was performed on data taken at center-of-mass energies of 161, 172 and 183 GeV, with integrated luminosities of 10.02, 9.97 and 52.0 pb^{-1} respectively. The event selection was divided into two steps. The first step involved selecting events having

the appropriate configuration, with a single shower in STIC and no signal in any other DELPHI subdetector. The second step consisted of using the veto counters to identify the showering particle in STIC as a photon.

3.1 Selection of Single-Photon Events

The selection of events with a single-photon candidate was based on the requirement that the events have exactly one electromagnetic shower in STIC and no signal anywhere else in DELPHI. The shower was required to have an energy E of at least 20 GeV. The absence of a signal anywhere else in DELPHI was established through the following criteria:

- There were no showers, other than the single-photon candidate, with an energy $E > 0.5$ GeV detected in STIC;
- There were no showers with an energy $E > 0.1$ GeV reconstructed in FEMC or in HPC;
- No charged-particle tracks had been reconstructed by any of the DELPHI tracking detectors;
- There were no showers with an energy $E > 0.5$ GeV detected in the hadronic calorimeter, HAC.

The efficiency of this event selection was 88% for the 183 GeV data sample, 97% for 172 GeV, and 95% GeV for 161 GeV. The efficiencies were estimated with a set of non-radiative Bhabha events in STIC. They were also estimated with a set of events triggered by the DELPHI random trigger; these efficiencies were slightly lower. This difference in efficiency between the two samples was taken into account in the estimation of the systematic errors. The efficiency at 183 GeV is lower than that of the other two energies because of a higher noise level in the HAC detector in 1997.

3.2 Identification of Photons

Once the single-photon candidates had been selected, further requirements were imposed on each event in order to identify the showering particle in STIC as a photon. Hence, it was required that the candidate event should have fired the neutral trigger. The trigger decision made on-line (see Section 2.2) is based on a set of discriminated signals from the veto counters. Off-line, ADC readings from the veto counters are also available, and these were used to refine the cut based on the neutral trigger.

The off-line cut was based on the same requirements as those of the neutral trigger, i.e., a shower in STIC in conjuntion with the absence of any signal in at least one of the scintillator planes in front of the shower, with the exception that both the ADC values and the discriminator values were used to identify a signal in the scintillators. A cut requiring the absence of any signal in either scintillator plane was tried, but this cut was found to veto many photons that had caused a backsplash (the so-called albedo) when entering the calorimeter.

The efficiency of the photon identification depends on the radius, and decreases at higher radii. This is due to the additional material, e.g., the TPC laser boxes, located there. The efficency ϵ has been parametrised as a function of polar angle [4], and is given by

$$\epsilon = -0.2475 + 0.3176 \cdot \theta - 0.03347 \cdot \theta^2,$$

where θ is measured in degrees. Due to the low photon-identification efficiency at high polar angles ($\epsilon \leq 0.10$ at $\theta \geq 8.2^\circ$), an upper cut at $\theta = 8^\circ$ was introduced in the analysis. The requirement of $r > 10$ cm in the neutral trigger sets a lower limit in polar angle at about $\theta = 2.8^\circ$ ($r \simeq 11$ cm).

4 Background

As mentioned already, the main type of background entering the single-photon sample is misidentified off-energy electrons. They are created in bremsstrahlung interactions between beam particles and residual gas molecules, and may have their origin anywhere in the beam line. Different methods to eliminate this background were studied; these are discussed in Section 4.1 below.

After the off-energy electrons, the largest contribution to background in the single-photon sample comes from the QED process $e^+e^- \to e^+e^-\gamma$, where the photon enters STIC and both electrons are lost in the beam pipe. This type of background is discussed further in Section 4.2 below.

A different configuration of radiative Bhabha scattering that likewise contributes to the background is that in which one of the electrons enters DELPHI and remains undetected. A brief account of this type of background is given in Section 4.3.

Other sources of background that were investigated but found to be of less or of no importance are cosmic events, Compton scattering on thermal photons, synchrotron radiation and detector noise. They are briefly discussed in Section 4.4.

4.1 Off-Energy Electron Background

Bremsstrahlung interactions between beam particles and residual gas molecules in the beam line create an abundance of electrons and photons. The photons produced in these interactions never reach DELPHI, but the electrons are bent into the STIC acceptance by the low-beta quadrupoles. The rate of this background is so high that, despite the fact that the veto counters have a rejection factor of ~ 1000, a large amount remained in the event samples after the event selection described above.

The off-energy electron background has been studied extensively elsewhere [6]. It was shown that the off-energy electrons are focused by the LEP quadrupoles into different azimuthal sectors of STIC in a very characteristic pattern. One horizontal and two vertical components can be distinguished. Each component has its own specific distributions in radius and in

energy. The horizontal component is confined to radii below 11 cm, whereas the vertical components extend to well over 20 cm in radius. The energy distributions scale linearly with the beam energy; they extend to about 50 GeV at $\sqrt{s} = 136$ GeV, and remain below 70 GeV at $\sqrt{s} = 183$ GeV. Figure 2 shows the two-dimensional radius-energy distributions of this background at $\sqrt{s} = 136$ GeV.

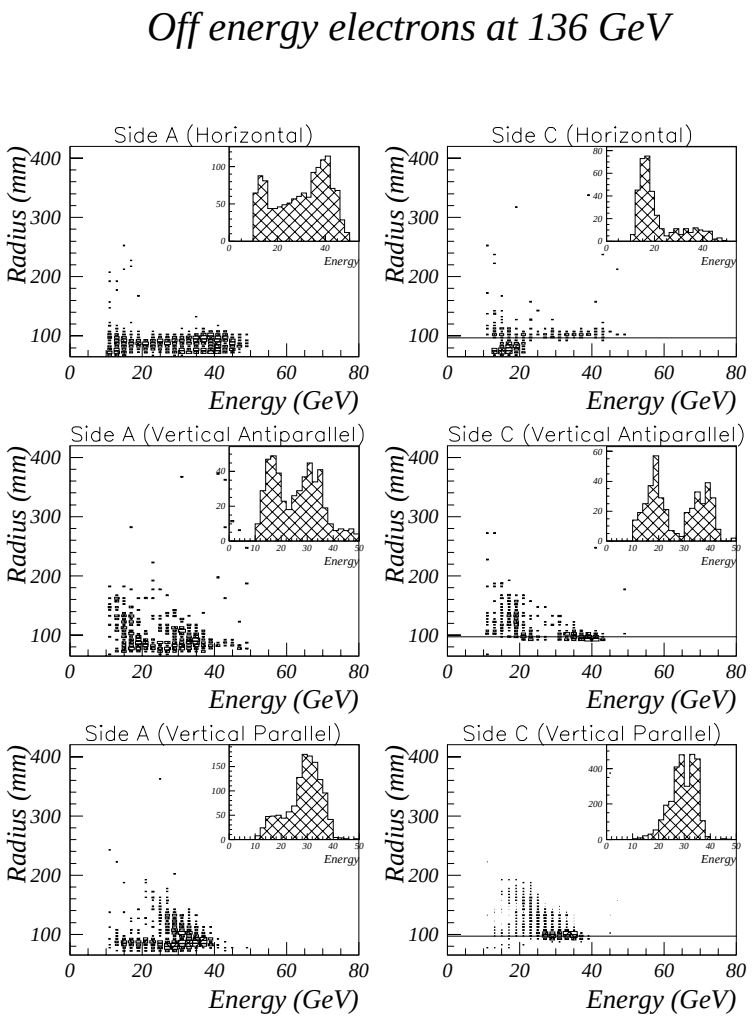

Figure 2: Distribution of radius *vs.* energy for off-energy electrons in STIC, at $\sqrt{s} = 136$ GeV. The three different components (horizontal, vertical antiparallel and vertical parallel) are shown for each calorimeter arm separately. The names "antiparallel" and "parallel" refer to the fact that these two components are deflected in a direction parallel or antiparallel to the direction of the electrostatic field that creates the vertical separation for the different bunches of the bunch trains in LEP. The C side was covered by a tungsten nose, extending to a radius $r = 97$ mm, during the 136 GeV data-taking. The edge of the tungsten nose is indicated by a line in the histograms.

The simulations in [6] showed good qualitative agreement with data. However, the Monte Carlo program used to simulate the off-energy electron events could not be used to estimate the

background quantitatively; its rate is highly dependent on the vacuum pressure in LEP, and this is generally not known to a good precision. Therefore, both the study of possible methods to eliminate this background, and the estimation of any remaining such background in the final data sample, were carried out with specially selected data samples consisting of single-electron events.

The single electrons were selected in a procedure similar to that of the single photons, but the veto counters were used to identify the showering particle as an electron. Hence, events were selected only if the neutral trigger had *not* been fired, and the off-line cut on the veto-counter ADCs and discriminators required a hit in both scintillator planes in the region around the entrance point of the showering particle (or, for the small veto counters, in at least one of the two scintillator halves); all other criteria were identical to those of the selection of single photons.

4.1.1 Methods to Remove the Off-Energy Electron Background

A polar-angular cut rejecting events below approximately 3° ($\simeq 12$ cm in radius) removes essentially all of the horizontal component of the off-energy electron background, and a good fraction of the vertical components as well. Two different methods to remove the remaining background in the vertical plane were tested: One was to combine the polar-angular cut with a cut on the vertex reconstructed by the silicon-strip detectors and with a cut in the $r-\varphi$ plane, where r is the radius and φ the azimuthal angle; the other was to tighten the cut on the polar angle.

The silicon-strip detectors have a reconstruction efficiency of about 90% [7]. A cut on the vertex at 75 cm on either side of the interaction point rejects 88% of the reconstructed off-energy electrons and keeps 73% of the particles originating from the interaction region. Choosing to retain particles whose vertices were not reconstructed, one obtains a total rejection of 79% and an efficiency of 76%. This cut is illustrated in Figure 3. Since the acceptance of the silicon detectors is limited to 17 cm in radius, it was necessary to introduce a cut in the $r-\varphi$ plane in order to remove background at higher radii. The cut was chosen to have, in the $x-y$ plane, the shape of two semi-ellipses joined along the horizontal axis. The horizontal axis of both ellipses is 6 cm, whereas the vertical axis is 22 cm in one case and 24 cm in the other; the reason for this is that the radial distributions are different for the two vertical background components. The $r-\varphi$ cut is illustrated in Figure 4. This combination of cuts removes nearly all of the background events that have an energy above a fraction $x_\gamma \simeq 0.4$ of the beam energy, but it necessitates further cuts in the low-energy region.

Using a combination of a cut on the reconstructed vertex and a cut in the $r-\varphi$ plane has the disadvantage of limiting the acceptance used for the cross section measurement, and also of yielding a lower efficiency in the region of the silicon detectors. If, however, these cuts are not carried out, one is obliged to tighten the polar-angular cut from $\sim 3^\circ$ to $\sim 4^\circ$ in order to remove the off-energy electron background.

At low energies, the QED background where both electrons were lost in the beam pipe eventually required a tighter cut than was necessary in order to remove the remaining off-energy

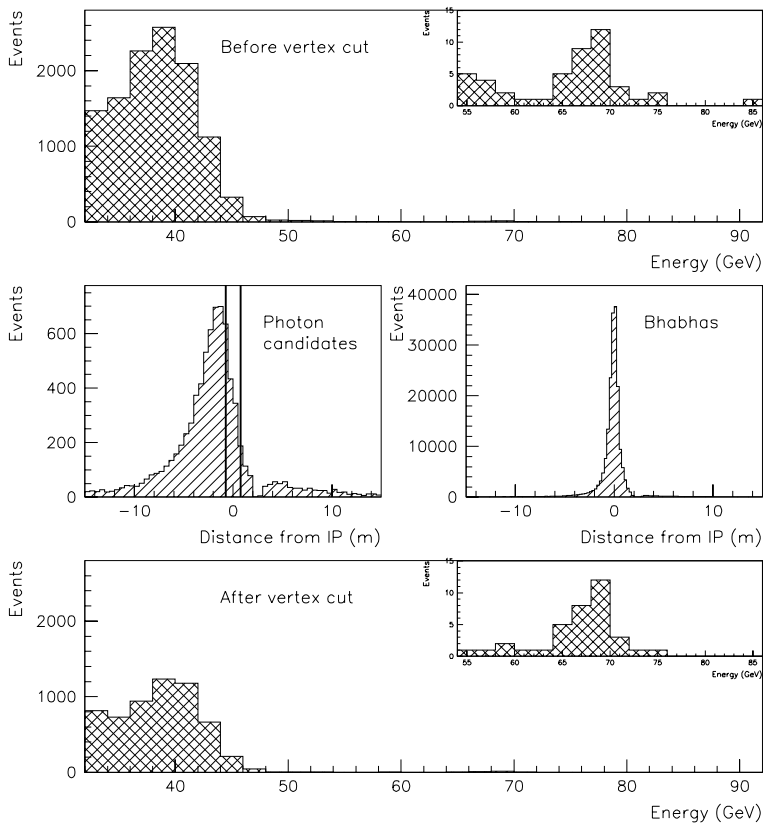

Figure 3: Illustration of the cut on the vertex reconstructed by the silicon-strip detectors. The figures in the center row show the distribution of reconstructed vertices for the sample of photon candidates at $\sqrt{s} = 183$ GeV, as well as that of a sample of Bhabha events, which are known to originate from the interaction point. Lines mark the cut at ± 75 cm on the vertices of the photon candidates. The top and bottom figures show the energy distributions of the photon candidates before and after the vertex cut.

electron background; this is discussed further in Section 4.2. Therefore, the best solution was to use a linear cut in the $x_\gamma - \theta$ plane in the region $0.3 \leq x_\gamma < 0.6$ and to omit entirely the region $x_\gamma < 0.3$, where it was not possible to obtain a satisfactory background rejection and where the efficiency of the neutral trigger was low. The two different methods developed into the following sets of cuts:

- Alternative 1: In the region $0.3 \leq x_\gamma < 0.6$, one uses the polar-angular acceptance $\theta_0 \leq \theta < 8.0°$, where θ_0 lies on the straight line between the points ($x_\gamma = 0.3$, $\theta = 6.5°$) and ($x_\gamma = 0.6$, $\theta = 4.2°$). Above $x_\gamma > 0.6$, one uses the polar-angular acceptance $4.2° - 8.0°$. These two areas will henceforth be called Region 1. In addition, Region 2 is defined by the cuts $x_\gamma > 0.6$ and $3.2° \leq \theta < 4.2°$. Region 1 has so little background contamination that it can be used without the vertex cut and the cut in the $r - \varphi$ plane. These cuts are, however, applied to Region 2.

- Alternative 2: Region 1 as described above is enlarged slightly for $\sqrt{s} = 183$ GeV and 172 GeV: the lower acceptance at $\theta = 4.2°$ is moved to $\theta = 3.8°$. For $\sqrt{s} = 161$ GeV, however, it remains at $\theta = 4.2°$. Region 2 is not used.

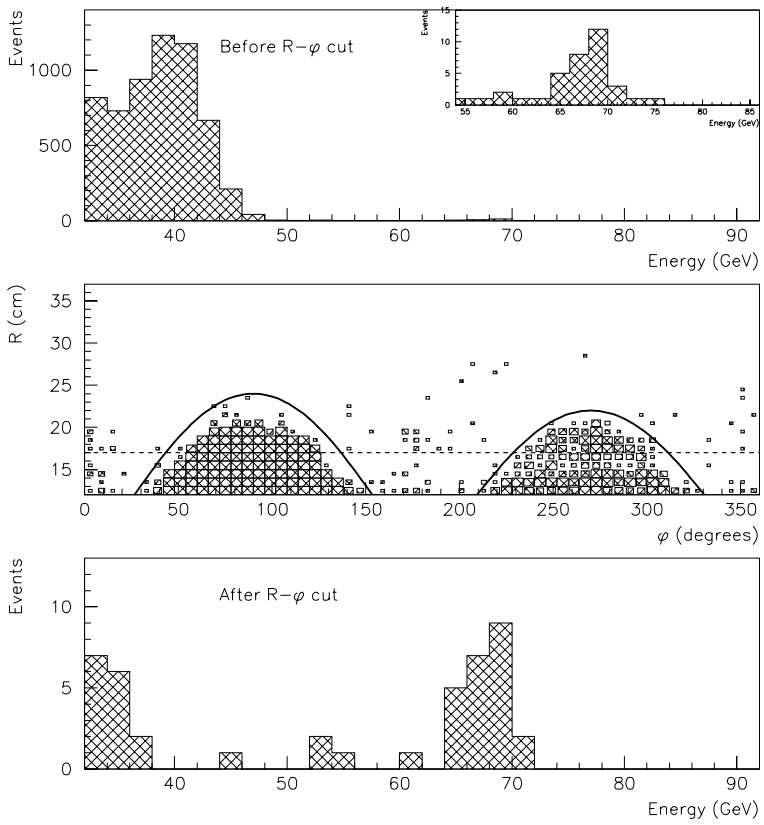

Figure 4: Illustration of the elliptical cut in the $r - \varphi$ plane. The center figure shows the two-dimensional distribution of the photon candidates in the $r - \varphi$ plane, for $\sqrt{s} = 183$ GeV. The curves drawn in the figure mark the cut. The dashed line shows the position of the outer edge of the silicon-strip detectors. The top and bottom figures show the energy distributions of the photon candidates before and after the $r - \varphi$ cut.

These two sets of cuts are illustrated in Figure 5.

4.1.2 Remaining Off-Energy Electron Background

The remaining off-energy electron background in the single-photon samples was estimated from the number of single-electron events surviving all of the selection cuts of the single-photon analysis, with the exception of the photon identification. This number was multiplied by a normalisation factor relating the size of the single-electron sample to the size of the single-photon sample. This factor was taken to be the ratio of single-photon candidates to single-electron events *inside* the ellipse described above; in both samples, the events in this region should come predominantly from off-energy electron background. At 183 GeV, the single-electron sample contained five times as many off-energy electrons as the single-photon sample. The final number of off-energy electron events contaminating the single-photon sample is shown, for each center-of-mass energy and each of the two analysis alternatives, in Table 1.

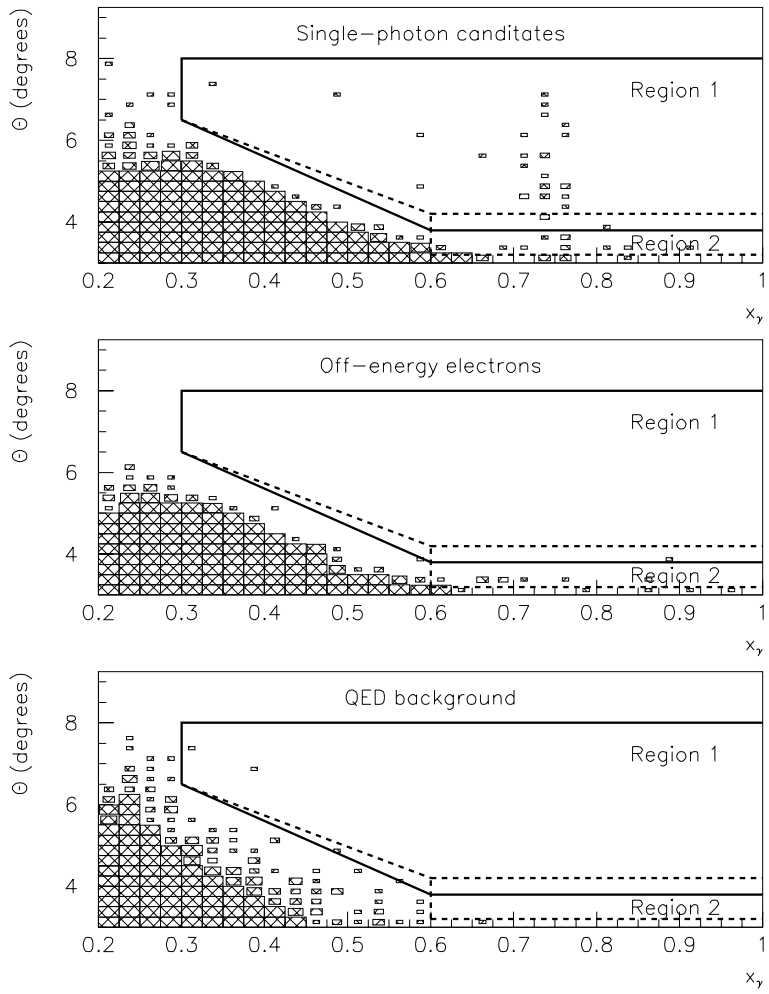

Figure 5: Polar angle *vs.* fraction of beam energy carried by the photon, for single-photon candidates (top), off-energy electron background (center), and simulated QED background (bottom), at $\sqrt{s} = 183$ GeV, after event selection and photon identification. The solid lines mark the boundaries of Region 1 used in the analysis without the silicon-strip detectors, i.e., in the final analysis. The dashed lines mark the boundaries of Region 1 and of Region 2 used in the analysis with the silicon-strip detectors. The number of events in each histogram corresponds to the integrated luminosity used in the analysis. A full box contains 10 events or more.

4.2 Background from QED with Both Electrons Lost in the Beam Pipe

The main source of photon background comes from the QED process $e^+e^- \to e^+e^-\gamma$, where the two electrons escape undetected along the beam pipe. One sometimes discriminates between radiative Bhabha scattering and Compton scattering, where Compton scattering indicates that the momentum transfer $q^2 \to 0$, i.e., the exchanged photon is (quasi)real and the scattering angle of one of the electrons is ~ 0.

The estimation of the QED background where the electrons are lost in the beam pipe was

CMS Energy	Analysis with Si-Strip Detectors		Analysis without Si-Strip Detectors	
	$0.3 \leq x_\gamma < 0.6$	$x_\gamma \geq 0.6$	$0.3 \leq x_\gamma < 0.6$	$x_\gamma \geq 0.6$
161 GeV	0	0	0	0
172 GeV	0	0	0	0
183 GeV	0	0.69 ± 0.40	0.23 ± 0.23	1.38 ± 0.56

Table 1: Number of events of off-energy electron background estimated to remain in the final data sample, for the three different center-of-mass energies and the two different analysis methods. The errors quoted are statistical.

done in two steps. DELSIM, the DELPHI detector simulation package [8], was used to establish the probability that an electron entering STIC would be detected, and hence that a QED event would be rejected, as a function of the polar angle at which it entered STIC. Radiative Bhabha scattering and Compton scattering events were then modeled with the Monte Carlo event generator TEEGG [9], which simulates the process $e^+e^- \to e^+e^-\gamma(\gamma)$ at low q^2. In this step, the detector response was not simulated; instead, the photon energy was smeared with a radius-dependent energy resolution corresponding to that measured previously with data.

The DELSIM studies, the results of which are shown in Figure 6, showed that the probability of detecting electrons at small polar angles varies considerably with the polar angle. Electrons entering the synchrotron mask inside the beam pipe, for instance, have a high probability of being detected due to energy leakage into the calorimeter. Electrons going through the tungsten shield have a probability of being detected varying from 0.1 to 1.0, depending on where they enter the shield and thus on the amount of material along their trajectories. Therefore, for the 183 GeV data, another cut was introduced, based on the data from the small veto counters in front of the tungsten shield. This required that no hits should have been recorded anywhere in the small veto counters, on either side. This cut removed some of the QED background at lower energies. A problem with corrupted discriminator/ADC information from the small veto counters prevented a similar cut in the 161 and 172 GeV analyses.

The simulations based on TEEGG showed that the energy spectrum of the photons coming from QED background of the type discussed here is highly dependent on the polar-angular region, and becomes softer with increasing polar angles. The two-dimensional $x_\gamma - \theta$ distribution of the simulated background is shown in Figure 5. This distribution has an almost triangular shape. The core of this type of QED background is confined to energies below $x_\gamma = 0.45$, and to polar angles below $\theta = 6.0^\circ$. However, small parts of it extend to high energies at low polar angles ($x_\gamma \simeq 0.7$ at $\theta \simeq 3^\circ$) and to large polar angles at low energies ($\theta \simeq 8^\circ$ at $x_\gamma \simeq 0.2$).

It was mainly the QED background that made it necessary to omit the region $x_\gamma < 0.3$. It was also, as mentioned in Section 4.1, the QED background that determined the linear cut in the $x_\gamma - \theta$ plane in the region $0.3 \leq x_\gamma < 0.6$. These two cuts removed most, but not all, of the QED background.

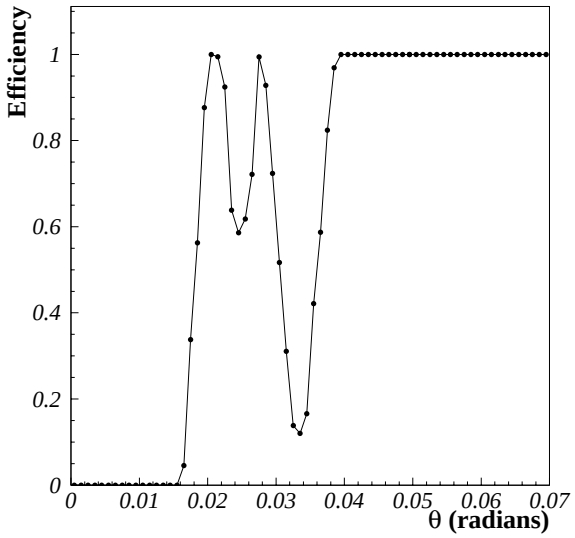

Figure 6: Probability of an electron being detected by STIC, as a function of the polar angle at which it enters the calorimeter. The electrons have an energy of 91.5 GeV, and the threshold for detection is 0.5 GeV. The peak in the efficiency at 0.020 comes from electrons showering in the synchrotron mask inside the beam pipe and leaking energy into STIC. The dip at 0.024 is due to electrons escaping below the calorimeter, whereas the peak at 0.027 is created by electrons entering STIC from below. The dip around 0.034 is caused by electrons entering the tungsten shield placed in front of STIC.

4.2.1 Remaining QED Background

The number of QED events with both electrons lost in the region below STIC that remained in the single-photon sample, after all cuts (including those of the two different methods described in Section 4.1) had been applied, was estimated with the TEEGG Monte Carlo samples. The results are shown in Table 2.

CMS Energy	Analysis with Si-Strip Detectors		Analysis without Si-Strip Detectors	
	$0.3 \leq x_\gamma < 0.6$	$x_\gamma \geq 0.6$	$0.3 \leq x_\gamma < 0.6$	$x_\gamma \geq 0.6$
161 GeV	0.10 ± 0.01	0.022 ± 0.005	0.10 ± 0.01	0
172 GeV	0.12 ± 0.02	0.005 ± 0.002	0.16 ± 0.02	0
183 GeV	0.12 ± 0.01	0.059 ± 0.008	0.20 ± 0.01	0.006 ± 0.002

Table 2: Estimated number of QED background events with both electrons escaping undetected that remain in the final data sample, for each of the three different center-of-mass energies and the two different analysis methods. The errors quoted are statistical.

4.3 Background from QED with One Electron Escaping Undetected in DELPHI

Radiative Bhabha scattering where one of the electrons enters DELPHI without being detected and the other is lost in the beam pipe also contributes to the background in the single-photon sample. This case was likewise studied with Monte Carlo simulations. TEEGG was used to generate $e^+e^-\gamma$ events with the photon in the STIC acceptance, the electron entering DELPHI above STIC ($\theta \geq 9^\circ$), and the positron escaping in the beam pipe. The electron (but not the photon) was then used as input to DELSIM. This configuration was seen to leave a contribution to the background in the region $x_\gamma \geq 0.6$. The quantitative estimate of the remaining background of this type in the different data samples is dealt with in Section 6, where the measured cross sections are discussed.

4.4 Other Sources of Background

Background types other than those discussed above were also investigated, but they were found to be of little or no importance to the single-photon analysis. They include cosmic events, Compton scattering on thermal photons, synchrotron radiation and detector noise.

Cosmic events sometimes give rise to single-photon candidates with a photon energy larger than the beam energy. These events were almost entirely eliminated by the requirement that no showers had been detected in HAC (see Section 3.1), and were assumed not to contribute to the background after that.

Compton scattering of beam particles on thermal photons in the beam pipe have been studied extensively at LEP [10]. These studies suggest that the average energy of the scattered photons is 2.2% of the beam energy at LEP2. This energy is too small for the photons to be seen in the analysis.

Photons originating from synchrotron radiation in the dipole and quadrupole fields of the LEP magnets have also been studied elsewhere [11], and have been found to have energies in the keV range. They are therefore of no concern to this analysis.

Detector noise has been observed to create fake events in STIC. The phototetrodes reading out the calorimeter occasionally generate large pulses, which give rise to clusters in the off-line shower reconstruction. These fake clusters were removed in the event selection by a requirement that a photon candidate should have a signal in at least nine adjacent towers. The efficiency of this selection criterion was estimated with data and Monte Carlo samples of hadronic radiative-return events ($e^+e^- \to \gamma + \text{hadrons}$) at 172 GeV. The efficiencies obtained were $96 \pm 2\%$ (data) and $99.0 \pm 0.1\%$ (Monte Carlo).

5 Comparison of Methods and Final Cuts

The two different sets of cuts discussed in the previous section gave very similar results in terms of number of events detected. The energy distributions, after imposing the cuts of each

method in turn, are shown in Figure 7. The rejection of off-energy electrons obtained with the cut on the vertex reconstructed by the silicon detectors was not sufficient to improve the analysis significantly. The rate of this type of background remained high even after the most seriously affected parts of the detector acceptance had been excluded with the $r-\varphi$ cut. It was not possible to enlarge further the region of phase space included in the analysis after the vertex and $r-\varphi$ cuts, and so the gain obtained by using the silicon detectors in the analysis was limited.

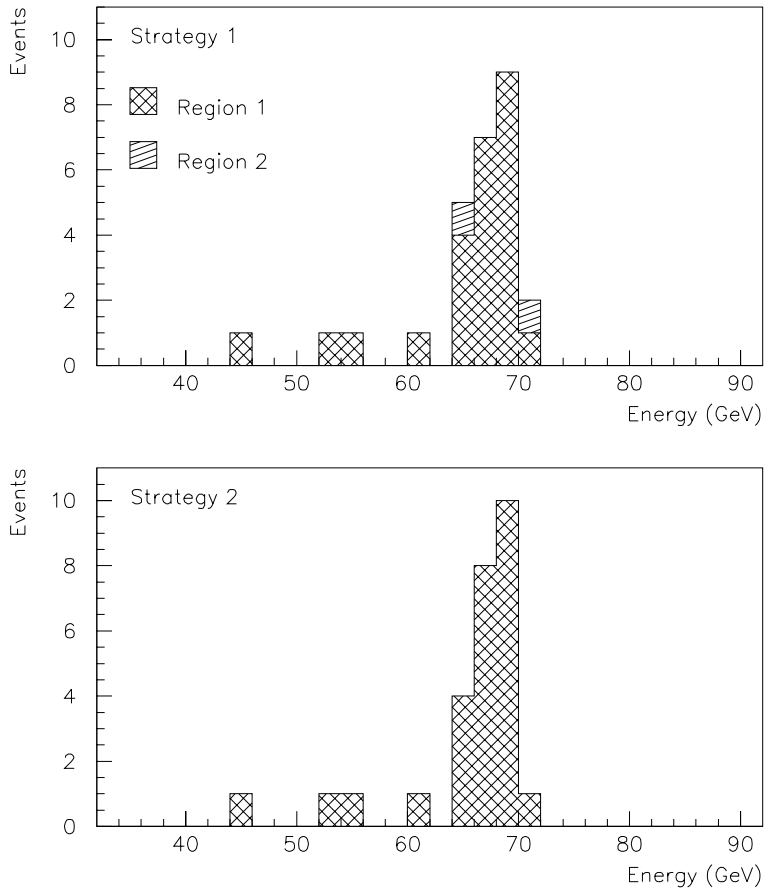

Figure 7: Energy distributions of single photons remaining when all cuts have been performed, for Regions 1 and 2 in the analysis with the silicon-strip detectors (top) and for Region 1 in the analysis without the silicon-strip detectors (bottom). $\sqrt{s} = 183$ GeV.

The total efficiencies of Regions 1 and 2, taking into account the efficiencies of the neutral trigger, the event selection, and the photon identification, and for Region 2 also the efficiencies of the vertex cut and of the $r-\varphi$ cut, depend on the photon energy and on the polar angle. An example, for a photon energy of 70 GeV, is shown in Figure 8. Due to the low efficiency of the cuts used in Region 2, one may argue that it is better to adopt the alternative using Region 1 only. This was the method chosen in a combined single-photon analysis at $\sqrt{s} = 183$ GeV, where STIC was one of the detectors used [1]. It is also the method used in the remainder of the analysis discussed here. The final cuts for each of the center-of-mass energies are listed in Table 3. The energy distributions of the final single-photon samples are shown in Figure 9.

CMS Energy	$0.3 \leq x_\gamma < 0.6$	$x_\gamma \geq 0.6$
161 GeV	$(6.5^\circ - 4.2^\circ) \cdot \frac{(x_\gamma - 0.6)}{(0.6-0.3)} + 6.5^\circ \leq \theta \leq 8.0^\circ$	$4.2^\circ \leq \theta \leq 8.0^\circ$
172 GeV	$(6.5^\circ - 3.8^\circ) \cdot \frac{(x_\gamma - 0.6)}{(0.6-0.3)} + 6.5^\circ \leq \theta \leq 8.0^\circ$	$3.8^\circ \leq \theta \leq 8.0^\circ$
183 GeV	$(6.5^\circ - 3.8^\circ) \cdot \frac{(x_\gamma - 0.6)}{(0.6-0.3)} + 6.5^\circ \leq \theta \leq 8.0^\circ$	$3.8^\circ \leq \theta \leq 8.0^\circ$

Table 3: Final cuts in the $x_\gamma - \theta$ plane, where x_γ is the fraction of the beam energy carried by the photon and θ the polar angle, for the different center-of-mass energies.

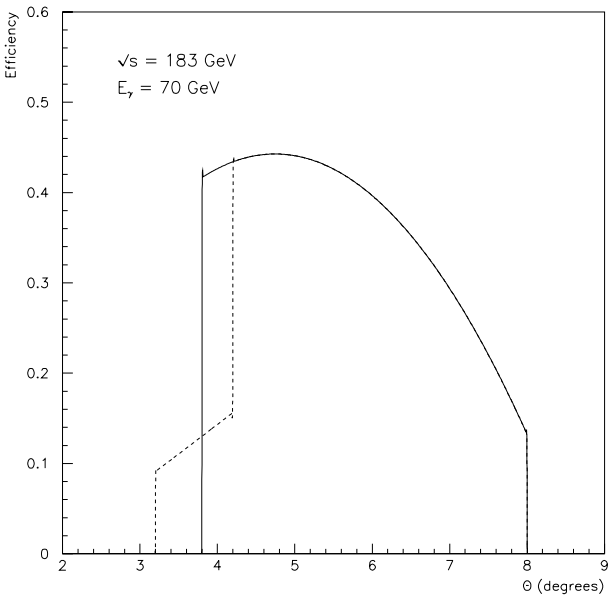

Figure 8: Total efficiency of the full selection procedure as a function of azimuthal angle measured by the calorimeter. The efficiency is shown for a photon energy of 70 GeV and a center-of-mass energy of 183 GeV. The continuous line shows the efficiency for Region 1 as defined in the final analysis, and the dashed line shows the efficiency for the modified Region 1 and the added Region 2. The total efficiency includes the efficiencies of the neutral trigger, the event selection, and the photon identification. For Region 2, it also includes the efficiencies of the vertex cut and the elliptical cut in the $r - \varphi$ plane.

6 Cross Sections

Events where the photon carries a fraction of the beam energy $x_\gamma \geq 0.6$ were selected for a measurement of the cross section in the radiative-return region. The measured efficiencies and background contributions were summed and used to calculate the cross section $\sigma(e^+e^- \to \gamma + \text{invisible})$ for each of the four center-of-mass energies. The results are shown in

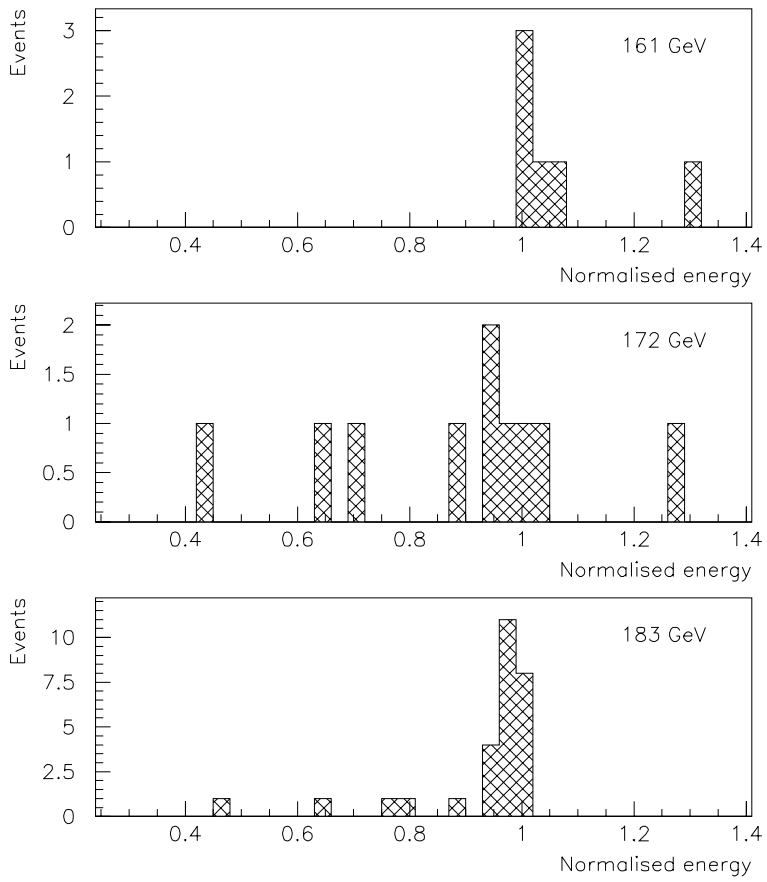

Figure 9: Energy distributions of the final single-photon samples (Region 1 only) for the different beam energies used in the analysis. The energy was normalised to that of the radiative-return peak for each data sample.

Table 4.

The systematic error of the measured cross sections is 11%. The dominant uncertainty comes from the estimation of identification and trigger efficiencies (7% and 6% respectively), together with the estimation of the remaining background (6%). Other sources of uncertainty are the luminosity (1%) and the energy scale of the calorimeter (1%). The individual errors were added in quadrature. They were considered to be the same for all three center-of-mass energies.

7 The Number of Neutrino Families

The cross sections measured for the single-photon production were compared to the theoretical cross sections for the process $e^+e^- \to \gamma\nu\bar{\nu}$. The number of neutrino families, N_ν, was calculated, under the assumption that the only contribution to the single-photon final state comes from neutrino production. The cross section for the process $e^+e^- \to \gamma\nu\bar{\nu}$ is directly proportional to the number of neutrino species.

CMS Energy	161 GeV	172 GeV	183 GeV
Int. Luminosity (pb^{-1})	10.02	9.97	52.0
Events	6 ± 2.4	7 ± 2.6	24 ± 4.9
Events/Efficiency	16.3 ± 6.6	17.1 ± 6.4	59.0 ± 12.0
Off-Energy Background	0	0	1.38 ± 0.56
QED Background I	0	0	0.006 ± 0.001
QED Background II	0.09 ± 0.09	0.09 ± 0.09	0.45 ± 0.45
Corr. Cross Section (pb)	1.60 ± 0.66	1.69 ± 0.65	1.08 ± 0.23

Table 4: Corrected cross sections for $e^+e^- \to \gamma +$ invisible in STIC at different center-of-mass energies. Only the region $x_\gamma \geq 0.6$ was used. QED Background I refers to the configuration in which both electrons are lost in the beam pipe, and QED Background II refers to that with one electron lost in the beam pipe and the other escaping undetected above STIC. The errors quoted are statistical.

The theoretical cross sections corresponding to the existence of three neutrino families were calculated with two different Monte Carlo event generators, NUNUGPV [12] and KORALZ [13]. The measured and the expected cross sections for the region $x_\gamma \geq 0.6$ of each center-of-mass energy are shown in Table 5. The cross sections calculated with KORALZ for this region are consistently lower than those calculated with NUNUGPV. A comparison of the energy distributions of the photon shows that the reason for this is that the distributions generated with KORALZ have a lower radiative-return peak with wider tails than the corresponding distributions generated with NUNUGPV. This difference is due to different ways in which the contribution from processes such as $e^+e^- \to \gamma\gamma\nu\bar{\nu}$, where one photon escapes undetected along the beam pipe, is calculated in the two event generators. The distributions generated with NUNUGPV seem to be in better agreement than those of KORALZ with the true photon distributions. A comparison between the energy distribution of the final event sample at $\sqrt{s} = 183$ GeV and the distribution predicted by NUNUGPV is shown in Figure 10.

NUNUGPV was used to determine the theoretical production cross sections for two, three and four neutrino families respectively. A straight line was fitted to the three points, and the number of neutrino families was determined from this line in combination with the corresponding measured cross section. This is illustrated in Figure 11. The number of neutrinos obtained at each center-of-mass energy is shown in Table 5. Averaging the number of neutrinos measured at the different center-of-mass energies, one obtains

$$N_\nu = 3.2 \pm 0.5 \pm 0.4.$$

The number of neutrino families calculated from the measurements with STIC at different center-of-mass energies are shown in Figure 12. For comparison, results obtained from other measurements with the FEMC and HPC calorimeters [1] are also shown. The significance of the STIC measurement is seen to be compatible with those from FEMC and HPC, despite the constraints imposed on the STIC analysis by the difficult background conditions.

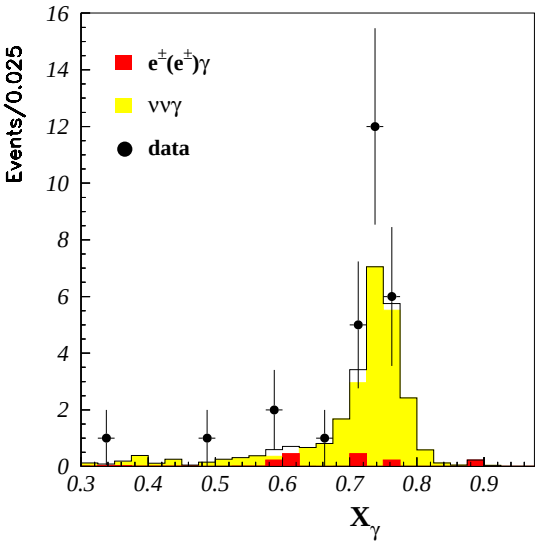

Figure 10: Energy distribution of the final event sample, together with the expected contribution from the process $e^+e^- \to \gamma\nu\bar{\nu}$ as calculated with NUNUGPV, and also with the contribution from the various background sources. $\sqrt{s} = 183$ GeV.

CMS Energy	Measured and Corrected Cross Section (pb)	Expected Cross Section (pb) NUNUGPV	KORALZ	Number of Neutrino Species
161 GeV	1.85 ± 0.76	1.46 ± 0.03	1.35 ± 0.03	3.80 ± 1.56
172 GeV	1.69 ± 0.65	1.26 ± 0.03	1.21 ± 0.03	4.02 ± 1.55
183 GeV	1.08 ± 0.23	1.09 ± 0.02	1.06 ± 0.03	2.97 ± 0.63

Table 5: Measured and expected cross sections for $e^+e^- \to \gamma\nu\bar{\nu}$, and the corresponding number of neutrino families, for the different center-of-mass energies. Only the region $x_\gamma \geq 0.6$ was used. The cross section at $\sqrt{s} = 161$ GeV is given for the same acceptance as the one at 172 and 183 GeV.

8 Conclusions

The calorimeter STIC has been used, for the first time, to identify and analyse events with a photon in the very forward region of DELPHI. Samples of single-photon events, where the photon had entered STIC, were analysed for center-of-mass energies of 161, 172, and 183 GeV. The single-photon events were used to explore the possibilites of using STIC to identify photons while maintaining control over the difficult background situation caused by the large number of off-energy electrons and by radiative Bhabha scattering.

A satisfactory background rejection was obtained with a set of cuts on the polar-angular acceptance and on the fraction of the beam energy carried by the photon. A combination of a cut on the vertex reconstructed by the STIC silicon detectors and a cut in the $r - \varphi$ plane was

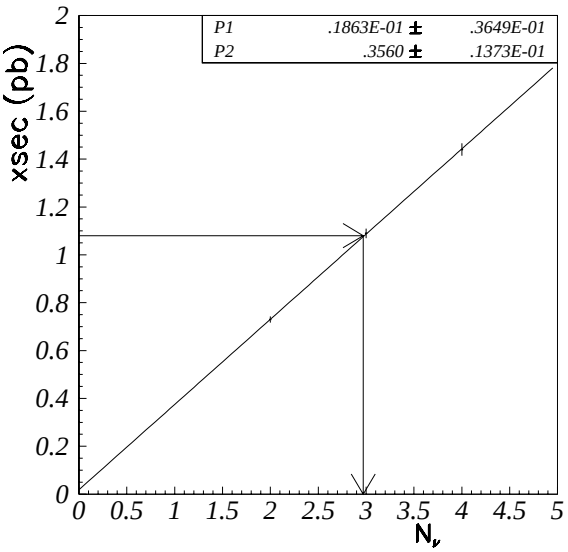

Figure 11: Theoretical cross section, as a function of the number of neutrino families, N_ν, for $\sqrt{s} = 183$ GeV. The cross sections for two, three and four neutrino families were calculated with NUNUGPV, and a straight line was fitted to the points. As the arrows indicate, the measured cross section, 1.09 pb, corresponds to $N_\nu = 2.97$.

tried and would have allowed the use of a somewhat larger region of phase space. However, the added region did not improve the significance of the analysis.

The measured cross sections for single-photon production were compared with the theoretical predictions for the process $e^+e^- \to \gamma\nu\bar{\nu}$ of two different Monte Carlo event generators, NUNUGPV and KORALZ. NUNUGPV was found to have a somewhat better agreement with data and was used to calculate the number of neutrino families.

The results of the measurement of the number of neutrino families were compared with those obtained from single-photon analyses carried out with the FEMC and HPC calorimeters. The results from STIC were competitive with those of FEMC and HPC, despite the very difficult background situation.

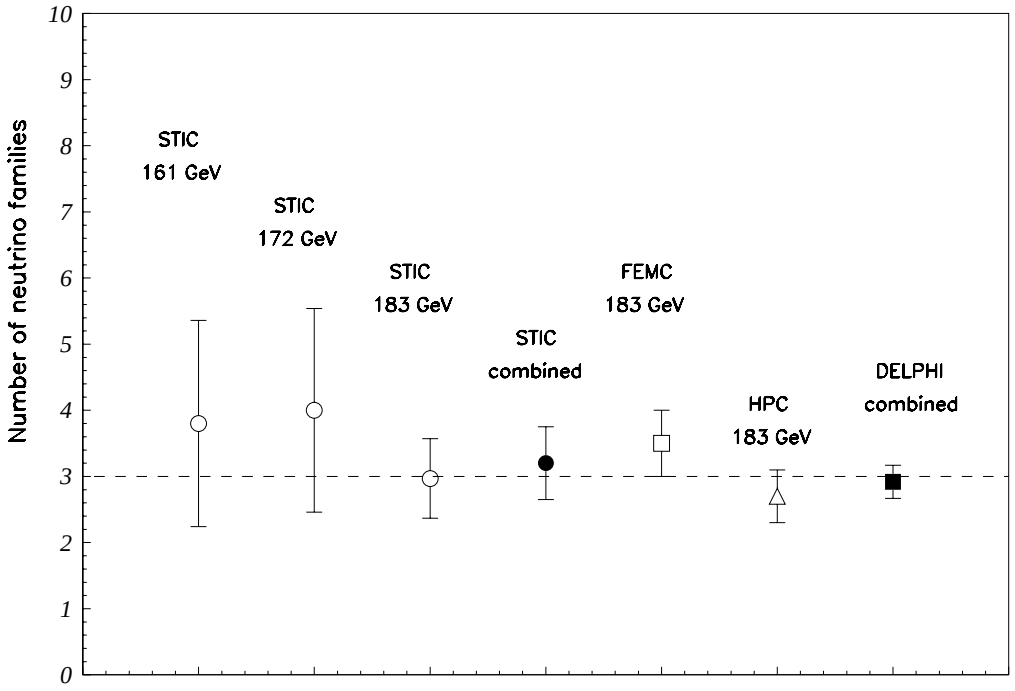

Figure 12: Number of neutrino families measured with STIC at different center-of-mass energies, together with the result of the individual measurements combined. For comparison, results obtained from measurements with the FEMC and HPC calorimeters, as well as the number obtained from combining all measurements with the three calorimeters, are also shown.

References

[1] E. Falk *et al.*, DELPHI 98-55 PHYS 780.

[2] DELPHI Collaboration, P. Abreu *et al.*, Eur. Phys. J. C1 (1998) 1;
DELPHI Collaboration, P. Abreu *et al.*, Phys. Lett. B380 (1996) 471;
DELPHI Collaboration, P. Abreu *et al.*, Z. Phys. C74 (1997) 577.

[3] S.J. Alvsvaag *et al.*, Nucl. Phys. B, Proc. Suppl. 44 (1995) 116; also available as DELPHI 95-12 CAL 119;
S.J. Alvsvaag *et al.*, IEEE Trans. Nucl. Sci. 42 (4) (1995) 478; also available as DELPHI 94-157 CAL 120;
S.J. Alvsvaag *et al.*, in H.A. Gordon and D. Rueger, eds., "Proceedings of the 5th International Conference on Calorimetry", World Scientific Publishing Co., Singapore 1995; also available as DELPHI 94-148 CAL 118;
S.J. Alvsvaag *et al.*, in H.S. Chen, ed., "Proceedings of the Beijing Calorimetry Symposium", IHEP, Beijing 1995; also available as DELPHI 95-14 CAL 123.

[4] P. Ferrari and V. Hedberg, DELPHI 98-49 CAL 141.

[5] S.J. Alvsvaag *et al.*, Nucl. Inst. and Meth. A360 (1995) 219; also available as DELPHI 94-126 CAL 117;
S.J. Alvsvaag *et al.*, IEEE Trans. Nucl. Sci. 42 (4) (1995) 469; also available as DELPHI 94-158 CAL 121;
S.J. Alvsvaag *et al.*, DELPHI 95-13 CAL 122; contribution to the 4th International Conference on Advanced Technology and Particle Physics, Como, Italy, October 1994.

[6] E. Falk, V. Hedberg and G. von Holtey, DELPHI 97-12 LEDI 8; also available as CERN SL/97-04 (EA).

[7] E. Falk, V. Hedberg and I. Gouz, DELPHI 98-43 CAL 140.

[8] DELPHI collaboration, DELPHI 89-67 PROG 142;
DELPHI collaboration, DELPHI 89-68 PROG 143.

[9] D. Karlen, Nucl. Phys. B289 (1987) 23.

[10] V.I. Telnov, Nucl. Inst. and Meth. A260 (1987) 304;
B. Dehning *et al.*, Phys. Lett. B249 (1990) 145;
C. Bini *et al.*, Phys. Lett. B262 (1991) 135;
C. Bini *et al.*, Nucl. Inst. and Meth. A306 (1991) 467;
H. Burkhardt, SL note 93-73;
G. von Holtey *et al.*, CERN-SL/97-40 (EA).

[11] G. von Holtey, CERN SL/95-29 (EA).

[12] G. Montagna *et al.*, Nucl. Phys. B452 (1995) 161.

[13] S. Jadach *et al.*, Comp. Phys. Comm. 66 (1991) 276;
S. Jadach *et al.*, Comp. Phys. Comm. 79 (1994) 503.